

# Highly Selective Oxidation of Carbohydrates in an Efficient Electrochemical Energy Converter: Cogenerating Organic Electrosynthesis

Yaovi Holade,<sup>[a]</sup> Karine Servat,<sup>[a]</sup> Teko W. Napporn,<sup>[a]</sup> Cláudia Morais,<sup>[a]</sup> Jean-Marc Berjeaud,<sup>[b]</sup> and Kouakou B. Kokoh<sup>\*[a]</sup>

The selective electrochemical conversion of highly functionalized organic molecules into electricity, heat, and added-value chemicals for fine chemistry requires the development of highly selective, durable, and low-cost catalysts. Here, we propose an approach to make catalysts that can convert carbohydrates into chemicals selectively and produce electrical power and recoverable heat. A 100% Faradaic yield was achieved for the selective oxidation of the anomeric carbon of glucose and its related carbohydrates (C1-position) without any function

protection. Furthermore, the direct glucose fuel cell (DGFC) enables an open-circuit voltage of 1.1 V in 0.5 M NaOH to be reached, a record. The optimized DGFC delivers an outstanding output power  $P_{\max} = 2 \text{ mW cm}^{-2}$  with the selective conversion of 0.3 M glucose, which is of great interest for cogeneration. The purified reaction product will serve as a raw material in various industries, which thereby reduces the cost of the whole sustainable process.

## Introduction

Energy converters are used with the aim to supply stationary and mobile devices with the minimum environmental impact.<sup>[1]</sup> In this frame, the development of renewable and low-cost energy sources is emerging to reduce our energy dependence on fossil fuels.<sup>[2]</sup> Notably, carbohydrates derived from biomass are abundant, renewable, and nontoxic organic compounds that have a potentially high energy.<sup>[3]</sup> Indeed, carbohydrates (glucose, etc), cellulose, and hemicellulose represent up to 70% of biomass (an extensive and endlessly renewable resource).<sup>[3a,4]</sup> Heterogeneous and enzymatic catalyzes have focused on the selective glucose oxidation to gluconic acid, a mild organic acid that has received tremendous interest in various fields (annual production  $\approx 100\,000 \text{ t}$ ) as its derivatives ( $\delta/\gamma$ -gluconolactone, sodium and calcium salts) are used in the food, pharmaceutical, and cosmetic industries.<sup>[5]</sup> Therefore, the search for highly selective catalysts to oxidize the hemiacetal function exclusively at the carbon C1-position (Figure S1 a) has become a prerequisite. The effective development of an efficient direct glucose fuel cell (DGFC), however, is hampered by the design of durable alkaline anion-exchange mem-

branes (AEM) as well as the synthesis of advanced electrode materials. In a DGFC, the fuel (fed directly into the anode without any previous chemical modification) is oxidized directly on the anode.<sup>[6]</sup> Indeed, the AEM (mostly from Solvay and Tokuyama) must withstand the strong alkalinity of the solution.<sup>[6a,7]</sup> The effectiveness of an AEM in solid alkaline membrane fuel cells (SAMFCs), however, is linked directly to the experimental conditions (fuel, temperature, etc),<sup>[6a,7c-e,8]</sup> and better performances for Fumatech are observed at low temperatures (such as those used for carbohydrate-based SAMFCs:  $< 50^\circ\text{C}$ ).<sup>[8]</sup>

The anode catalyst must withstand the poisoning effect of species adsorbed strongly that come from the oxidation of organics, and the cathode must be able to overcome the sluggishness of the oxygen reduction reaction (ORR).<sup>[9]</sup> A simplified Pourbaix diagram of glucose in aqueous medium based on thermodynamic data is shown in Figure 1 (left y axis).<sup>[10]</sup> This displays the open-circuit potential (OCP) of the ORR and the glucose oxidation reaction (GOR) with two exchanged electrons ( $n_{\text{ex}} = 2$ ). The potentials are referenced to the standard hydrogen electrode (SHE), whereas those scaled to the saturated calomel electrode (SCE), silver/silver chloride electrode (SSCE), and reversible hydrogen electrode (RHE) are reported in Figure S1. For the ORR, the OCP is  $\approx 1.18 \text{ V}$  vs. RHE in aqueous solutions. Recently, advances in materials science have allowed the preparation of active catalysts able to deliver an OCP  $> 1 \text{ V}$  vs. RHE (overpotential  $< 200 \text{ mV}$ ) with good kinetics at 0.8–0.95 V vs. RHE.<sup>[9b,11]</sup> However, the most challenging issue for SAMFCs is the anodic reaction. To date, the oxidation of organic molecule at the anode, even with the most active nanocatalyst, largely occurs with an overpotential  $\geq 200 \text{ mV}$ , and activation is very difficult. Theoretically, at pH 14, the OCP is  $-1.12 \text{ V}$  vs. SHE or  $-0.294 \text{ V}$  vs. RHE for the GOR. Unfortunate-

[a] Dr. Y. Holade, Dr. K. Servat, Dr. T. W. Napporn, Dr. C. Morais,  
Prof. Dr. K. B. Kokoh  
Department of Chemistry  
IC2MP CNRS UMR 7285  
Université de Poitiers  
4 rue Michel Brunet - B27, TSA 51106, 86073 Cedex 9 (France)  
E-mail: boniface.kokoh@univ-poitiers.fr

[b] Prof. Dr. J.-M. Berjeaud  
EBI UMR 7267 CNRS  
Université de Poitiers  
1 rue Georges Bonnet, B36/37, TSA 51106, 86073 Poitiers cedex 09 (France)

Supporting Information for this article is available on the WWW under <http://dx.doi.org/10.1002/cssc.201501593>.

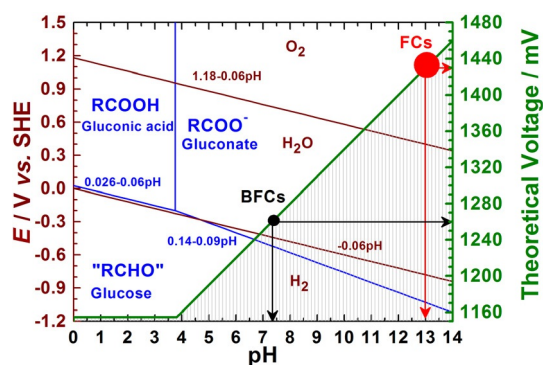


**Figure 1.** From glucose to electrochemical energy: direct alkaline fuel cell. Left y axis: simplified Pourbaix diagrams for glucose (blue lines) and water (brown lines) systems. Right y axis: theoretically recoverable voltage, OCV (green line); the dashed zone shows the possible values.

ly, Pt, which allows an OCP of  $\approx +0.05$  V vs. RHE (most dehydrogenation catalysts), is deactivated rapidly. The compromise relies on Pt-based electrocatalysts. Still out of control, the reaction induces C–C bond cleavage to lead to unrecoverable products that also deactivate the catalyst. Thorough glucose electro-oxidation involves 24 electrons per molecule and enables an OCV of 1.25 V to be harvested, which constitutes a free energy of  $2871 \text{ kJ mol}^{-1}$ , that is,  $4.430 \text{ kWh kg}^{-1}$ .<sup>[3a,6a,12]</sup>

As indicated above, the last few decades of research has dealt with  $n_{\text{ex}}=2$  towards gluconic acid ( $pK_a=3.76$ ). Therefore, as charted in Figure 1 (right y axis), the electrochemical conversion of glucose as a sustainable fuel affords  $\text{OCV}=1.154$  V for  $\text{pH}\leq 3.76$  and  $\text{OCV}=1.04+0.03\times\text{pH}$  for  $\text{pH}\geq 3.76$ . Particular operating points highlighted in Figure 1 (black for biofuel cells (BFCs)<sup>[13]</sup> and red for DGFCs) arise as the two new paradigms in the GOR to value electricity. Thus, a specific energy of  $0.435 \text{ kWh kg}^{-1}$  is expected at pH 14. Even if it represents only  $\approx 10\%$  of the value from the total glucose oxidation, the concept is better as gluconate (thus, gluconic acid) is a high added-value product compared to carbonate from total oxidation. Currently, DGFCs that use an AEM or not deliver a maximum output power density  $P_{\text{max}}$  of  $0.5\text{--}1.5 \text{ mW cm}^{-2}$ . Surprisingly, Fujiwara et al.<sup>[14]</sup> reported a DGFC designed with an AEM that delivers a  $P_{\text{max}}$  of  $20 \text{ mW cm}^{-2}$  at  $30^\circ\text{C}$  in  $0.5 \text{ M KOH}$  with  $0.5 \text{ M}$  glucose that contained a high metal loading of  $3 \text{ mg}_{\text{metal}}\text{cm}^{-2}$  (carbon-free PtRu (cathode) and Pt nanoparticles (anode)). With regard to the scarcity and high price of Pt and Ru, this kind of design requires noble metal reduction in the electrode catalysts.<sup>[11a]</sup> No stability test was performed as the anode material (Pt) is deactivated swiftly by reaction intermediates. Our main goal herein is to prove the feasibility of the electrochemical cogeneration process by harvesting electrical power as the fuel is oxidized selectively to added-value chemicals. For this purpose, highly active and selective Au nanoparticles were prepared as the anode catalyst from a simple method without surfactant. For the first time, a unique final product was determined from a versatile experimental setup thanks to the careful and judicious coupling of electrochemistry to analytical chemistry.

## Results and Discussion

A broad overview of this study with major goals is provided in Scheme S1 in the Supporting Information.

### Au nanomaterials characterization by TEM and X-ray photoelectron spectroscopy and their electrocatalytic activity

Typical TEM images of the Au/C nanocatalyst are shown in Figure 2 (panels i–iv). The total metal loading determined from thermogravimetric analysis (TGA; Figure S2a) is 21 wt% as expected (theoretical: 20 wt%). The average particle size is  $(5.7\pm 0.1) \text{ nm}$  as can be seen from the histograms presented inset in Figure 2 (panel i). Basically, the nanocrystals are deposited randomly onto the support without a well-defined orientation. The high-resolution transmission electron microscopy (HRTEM) micrographs shown in Figure 2 (panels v–vi) display a truncated octahedral shape with different degrees of truncation. The nanoparticles have facets oriented along the (111) and (200) crystallographic planes instead of the common (111) and (100) planes predicted by Wulff's theorem.

We further characterized the Au/C surface state by X-ray photoelectron spectroscopy (XPS). The high-resolution XPS spectrum of the Au 4f region is depicted in Figure 3a. The observed doublets are related to spin–orbit splitting ( $\pm 1/2$ ). The doublets of Au are situated at binding energies (BEs) of 83.9 (Au 4f<sub>7/2</sub>) and 87.6 eV (Au 4f<sub>5/2</sub>).<sup>[15]</sup> The presence of oxide AuO<sub>x</sub> is indicated by doublets at BE=85.5 (Au 4f<sub>7/2</sub>) and 89.1 eV (Au 4f<sub>5/2</sub>). Energy-dispersive X-ray (EDX) spectroscopy and XRD (Figure S2b–c) agree completely that the oxide amount is negligible. Currently, upon exposure to ambient air, a thin protective layer safeguards the metal surface from deep oxidation (passivation layer).

The electrochemical behavior of Au/C in  $0.1 \text{ M NaOH}$  is shown in Figure 3b (dashed plots). Two major features during the positive scan (peak A': metal oxidation) and the negative scan (peak C': oxide reduction) typify Au in an alkaline medium.<sup>[15–16]</sup> In the presence of  $10 \text{ mM}$  glucose, the electrocatalytic oxidation of glucose is marked by peaks A<sub>1</sub>, A<sub>2</sub>, A<sub>3</sub> (forward), and C<sub>1</sub> (backward). These peaks are well displayed in Figure S3. Notably, the oxidation peak A<sub>2</sub> is associated with a shoulder around 0.9 V vs. RHE. This shoulder is situated in the potential range in which the adsorption of hydroxyl species occurs at the Au surface. Actually, glucose electro-oxidation at the Au/C catalyst surface involves three different species of Au: Au metal (peak A<sub>1</sub>~0.5 V vs. RHE), Au(OH)<sub>x</sub> (peak A<sub>2</sub>~1.2 V vs. RHE), and AuO<sub>x</sub> (peaks A<sub>3</sub>~1.3 V vs. RHE and C<sub>1</sub>~1.2 V vs. RHE). The phenomenon that is marked by the peak A<sub>2</sub> is initiated from the shoulder at around 0.9 V vs. RHE. The main phenomena that occur at these peaks will be determined thoroughly later. The onset potential is  $\approx 0.2$  V vs. RHE, which correlates roughly to 0.49 V of overpotential. However, previous studies show that the GOR starts here at least 100 mV earlier.<sup>[17]</sup> The current density is  $285 \text{ A cm}^{-2}\text{g}^{-1}$  ( $20 \text{ A g}^{-1}$  or  $2 \text{ mA cm}^{-2}$ ) at 0.5 V vs. RHE and  $1025 \text{ A cm}^{-2}\text{g}^{-1}$  (i.e.,  $72 \text{ A g}^{-1}$  or  $6 \text{ mA cm}^{-2}$ ) at the peak, that is, 1.2 V vs. RHE. Here, the catalyst shows superior electrocatalytic activity because of its good

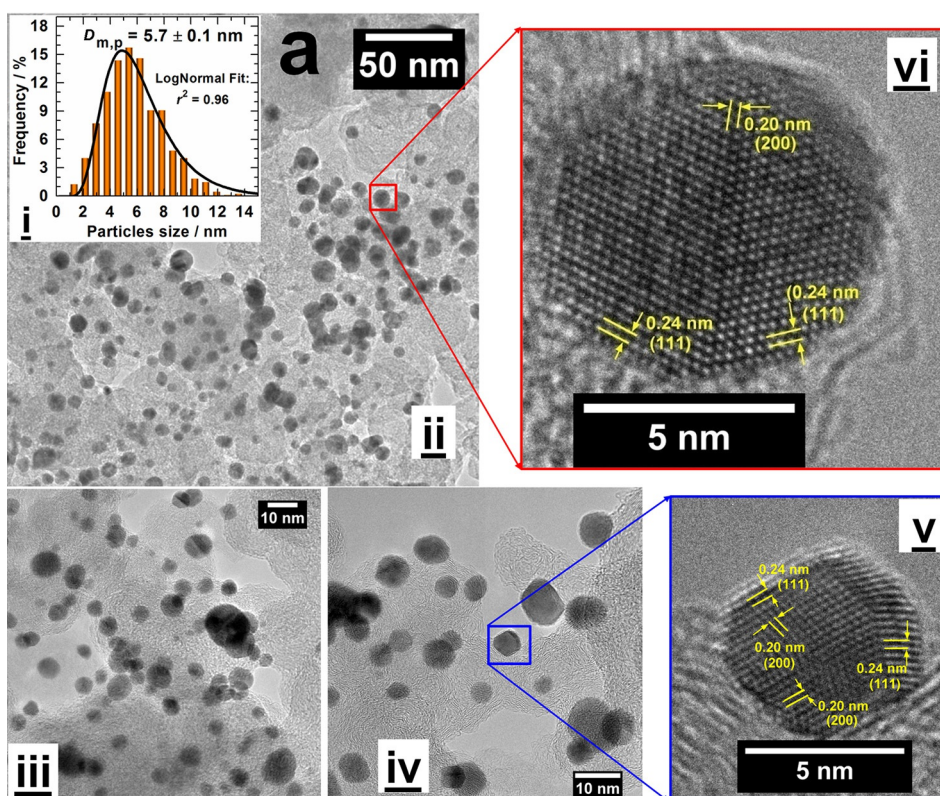


**Figure 2.** TEM images of gold nanoparticles dispersed on Vulcan XC 72R carbon (Au/C, 20 wt %) with different magnifications and i) the histogram of nanoparticle size distribution (inset). ii) Overview (50 nm scale bar), iii–iv) near view (10 nm scale bar), and v–vi) close view that shows HRTEM micrographs of one nanoparticle (zone axis: [101]).

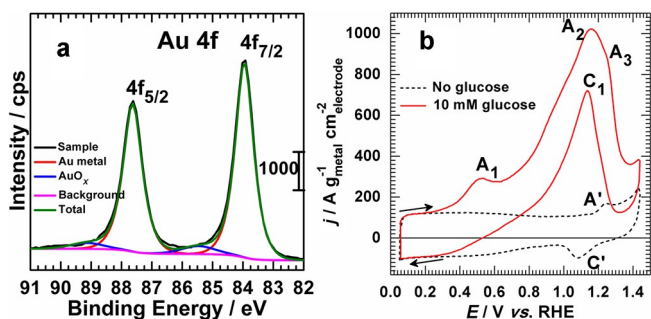


**Figure 3.** a) High-resolution XPS spectra of the Au 4f core level of gold nanoparticles dispersed on Vulcan XC 72R carbon. b) CVs of a Au/C electrode material at  $20 \text{ mV s}^{-1}$  in a  $0.1 \text{ mol L}^{-1}$  NaOH electrolytic solution at  $25^\circ \text{C}$  in the absence (black dashed line) and presence of  $10 \text{ mmol L}^{-1}$  glucose (solid red line).

kinetics compared to that in previous studies.<sup>[17]</sup> The scan rate effect on the Au/C electrode material is reported in Figure S3. The analysis indicates that the electrochemical processes are mainly under the diffusion control of the reactants and/or products with a substantial contribution from adsorption. Independent investigation by the temperature effect has shown that the electrochemical activation energy is less than  $50 \text{ kJ mol}^{-1}$ ; which thereby endorses our conclusion. Before a DGFC is designed, methods of chemical analysis will be coupled with electrochemical methods for the determination of the reaction products that result from the electrocatalytic oxi-

dation of glucose in alkaline media. We first postulate that the GOR might concern the aldehyde function (C1-position:  $n_{\text{ex}} = 2$ ), the primary alcohol (C6-position:  $n_{\text{ex}} = 4$ ), or both ( $n_{\text{ex}} = 6$ ).

### Spectroelectrochemical determination of the reaction intermediates and products

#### Cyclic voltammetry coupled with IR spectroscopy: CV-FTIRS (SPAIRS)

To prove our previous hypothesis ( $n_{\text{ex}} \leq 6$ ), we recorded FTIR spectra of glucose and different possible intermediates or products in  $0.1 \text{ M}$  NaOH as references for band assignment. The chemical structures of these possible reaction intermediates or products are displayed in Figure S4, their reflectance FTIR spectra are shown in Figure S5a, and the main characteristics are summarized in Table S1. Finally, concentrated standards were used to better discern bands as no significant effect on their position was observed during preliminary tests (Figure S5b). Preliminary optimized GOR conditions based on glucose concentration ( $10\text{--}100 \text{ mM}$ ) and using the state-of-the-art Pt/C catalyst are given in Figure S6a–e. However, very low concentrations give a low amount of reaction products so it will be difficult to identify them by IR spectroscopy. Therefore,  $50 \text{ mM}$  glucose was used. The single potential alteration infrared spectroscopy (SPAIRS) results are shown in Figure 4. The CV shown in Figure 4a displays the forward-going process (red

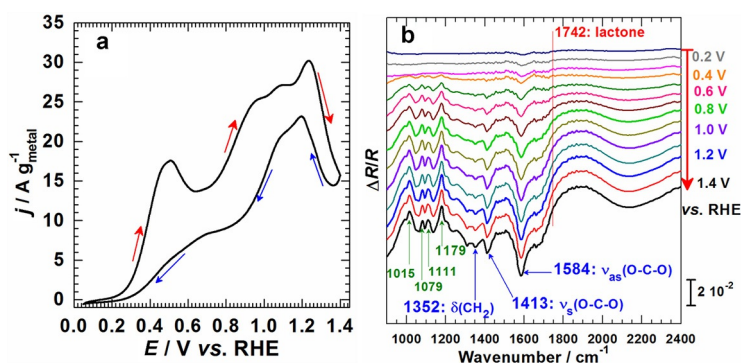


**Figure 4.** CV-FTIRS experiments on a Au/C electrode material at a scan rate of  $1 \text{ mV s}^{-1}$  in  $0.1 \text{ mol L}^{-1} \text{ NaOH} + 50 \text{ mmol L}^{-1} \text{ glucose}$ : a) CVs recorded in the FTIRS cell and b) CV-FTIR spectra.

arrows) and reverse scan (blue arrows). FTIR spectra, plotted every  $0.1 \text{ V}$ , are depicted in Figure 4b for the positive scan ( $0.1\text{--}1.4 \text{ V}$  vs. RHE) and in Figure S6 f for the reverse scan ( $1.4\text{--}0.1 \text{ V}$  vs. RHE). Basically, for the in situ reflectance mode, a band that faces downward indicates the formation of a compound, whereas a band that faces upwards signifies its removal from the window–electrode interface (an intermediate or simple diffusion process). We underscore important current trends that voltammograms recorded in the IR cell are typical of those already obtained in a conventional electrochemical cell. Thus, all processes are typical of the reactions involved. During the positive scan, oxidation starts very early at  $E \leq 0.2 \text{ V}$  vs. RHE (Figure 4a), which thereby corroborates the results shown in Figure 3b. Accordingly, two bands that appear synchronously at approximately  $\tilde{\nu} = 1584$  and  $1413 \text{ cm}^{-1}$  can be seen in the spectra presented in Figure 4b. As indicated in Table S1, these bands correspond to the asymmetric stretching vibration  $\nu_{\text{as}}(\text{O-C-O})$  and symmetric  $\nu_{\text{s}}(\text{O-C-O})$  of  $\text{COO}^-$  (oxidized carbohydrate specific functions), respectively. Glucose consumption is indicated (through its dehydrogenated species) by the positive bands at approximately  $\tilde{\nu} = 1200$  (distortion band) and  $2500\text{--}2900 \text{ cm}^{-1}$  (stretching band). The amount of water in the thin electrolyte layer during the reaction is demonstrated by its  $\delta(\text{H}_2\text{O})$  band at approximately  $\tilde{\nu} = 1660 \text{ cm}^{-1}$ . The same bands are present in the reverse scan (Figure S6 f). The identification of the bands during the reverse scan is a challenge because the species are already in the solution (during the positive scan), so we performed a fresh experiment by starting at the upper potential ( $1.4 \text{ V}$  vs. RHE) for the precise and unequivocal determination of the nature of the processes that take place. Surprisingly, the results (not shown) showed a similar voltammogram and the same bands. These results, reported herein for the first time, mean that the peak observed during the reverse scan comes from glucose oxidation, not from intermediates adsorbed strongly (absent).

Furthermore, in-depth analysis of the spectra shows a dilemma for the assignment of the bands at  $\tilde{\nu} = 1413$  and  $1584 \text{ cm}^{-1}$ . Indeed, they could belong to gluconate (C1 oxidation), glucuronate (C6 oxida-

tion), or glucarate (both C1 and C6 oxidation). Otherwise, neither compound resulted in C–C bond cleavage ( $\text{CO}$ :  $\tilde{\nu} = 1900\text{--}2100 \text{ cm}^{-1}$ , carbonate:  $\tilde{\nu} = 1396 \text{ cm}^{-1}$ ,  $\text{CO}_2$ :  $\tilde{\nu} = 2340\text{--}2350 \text{ cm}^{-1}$ ) nor gluconolactone (specific  $\nu\text{C}=\text{O}$  band at  $\tilde{\nu} = 1742 \text{ cm}^{-1}$ ) are observed. The first assessment indicates a selective oxidation at the whole electrode potential range without C–C bond breaking and the last one highlights a fast gluconolactone hydrolysis as it is an unavoidable intermediate. Thereby, these results validate our initial hypothesis if we assume that  $n_{\text{ex}} \leq 6$ . Such observations indicate that our revisited bromide anion exchange (BAE) protocol changed the GOR kinetics drastically as both C–C bond cleavage and gluconolactone were observed by many methods if metal or enzymatic catalysts were used previously.<sup>[3a,18]</sup>

### Chronoamperometry coupled with IR spectroscopy: CA-FTIRS

The CA-FTIRS technique allows the online monitoring of the electrocatalytic reaction by following the vibration bands at a fixed electrode potential. CA-FTIRS investigations were performed at various electrode potentials from  $0.2$  to  $1.4 \text{ V}$  vs. RHE. Although CA results change from one potential to another (rational trend), we were surprised to find that the bands were unchanged. A CA plot for  $0.5 \text{ V}$  vs. RHE is shown in Figure 5a and its spectra are presented in Figure 5b. The intensity of the CA-FTIRS bands increases over time (an increase in conversion rate). Moreover, the spectra show the same bands as those from CV-FTIRS. All of the bands appear during the first minutes. The solution to the FTIRS dilemma about the bands at  $\tilde{\nu} = 1413$  and  $1584 \text{ cm}^{-1}$  consists of using complementary techniques using chromatography and spectroscopy in tandem.

### Electrosynthesis: Carbohydrate electrolysis

After the spectro-electrochemistry experiments, electrolysis was performed in potentiostatic mode by applying different electrode potentials from  $0.2$  to  $1 \text{ V}$  vs. RHE in preliminary tests. Chromatography analyses did not show any difference in

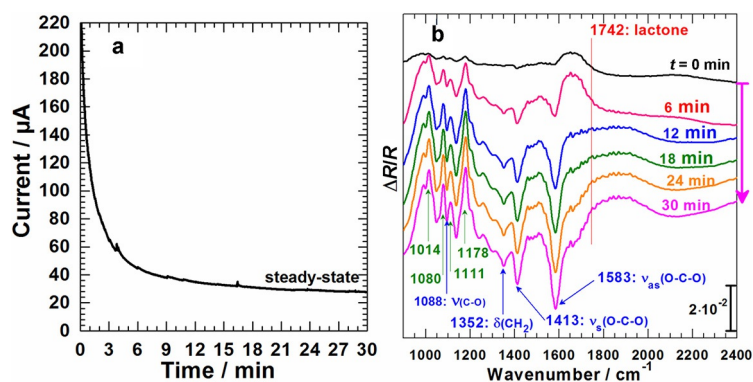


**Figure 5.** CA-FTIRS experiments on a Au/C electrode material at  $0.5 \text{ V}$  vs. RHE in  $0.1 \text{ mol L}^{-1} \text{ NaOH} + 50 \text{ mmol L}^{-1} \text{ glucose}$ : a) Chronoamperogram recorded in the FTIRS cell and b) CA-FTIR spectra plotted every 6 min.

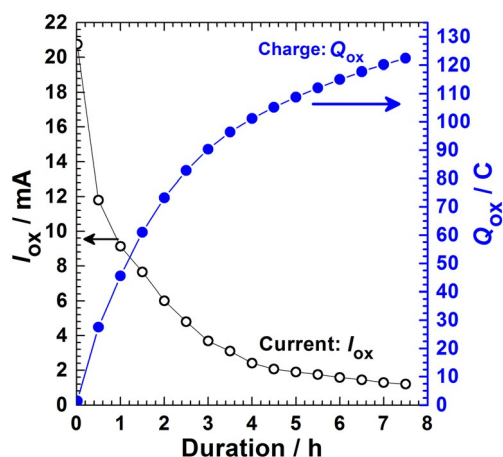


**Figure 6.** Electrolysis of 20 mmol L<sup>-1</sup> glucose in 0.1 mol L<sup>-1</sup> NaOH on a Au/C electrode material at 0.8 V vs. RHE. Oxidation current  $I_{ox}$  (left y axis, black open circles) and quantity of electricity  $Q_{ox}$  (Right y axis, blue solid circles).

the distribution of the reaction products. Consequently, the electrosynthesis experiment in this study concerns a process set at 0.8 V vs. RHE. The electrolysis of 20 mM glucose results in terms of oxidation current ( $I_{ox}$ , left y axis) and quantity of electricity ( $Q_{ox}$ , right y axis) are displayed in Figure 6. The progressive decrease in  $I_{ox}$  may be attributed reasonably to glucose consumption and/or to catalyst deactivation. Indeed, strongly adsorbed oxygenated species that come from GOR on the catalyst surface cause its deactivation even if Au is one the most stable catalysts for GOR. After 7.5 h of electrolysis, the produced quantity of electricity is  $Q_{ox} = 123$  C. Other carbohydrates were also studied;  $Q_{ox} = 131$  C for galactose (the isomer of glucose) and  $Q_{ox} = 87$  C for lactose (a dimer of glucose and galactose; Figure S7). More quantitative data will be extracted after chromatographic analyses.

#### High-performance liquid ionic chromatography: Identification of the product(s)

With the aim to determine exactly the nature of the final product(s), we performed high-performance liquid ionic chromatography (HPLIC). The chromatograms shown in Figure S8a indicate that the retention time ( $t_R$ ) is 5–6, 10, and 21 min for gluconate, glucuronate, and glucarate, respectively. The qualitative HPLIC analysis of the sample after electrolysis is depicted in Figure 7a, which highlights the presence of two unresolved peaks A ( $t_R = 5.5$  min) and B ( $t_R = 6.1$  min). As indicated, peak A belongs to gluconate. However, peak B does not belong either to glucuronate or glucarate. Seminal studies with bulk Au or Pt electrodes have shown that this peak belongs to gluconate, and other derivative compounds from C–C bond breaking were also identified.<sup>[18d,19]</sup> We combined in situ FTIRS studies and HPLIC analyses to be able to state unambiguously that C–C bond cleavage does not occur. It is possible that A and B both belong to gluconate. Other investiga-

tions will be undertaken to test this hypothesis. From the gluconate calibration plots (Figure S8b), its concentration ( $c$ ) was evaluated to be 13 mM after 7.4 h of electrolysis. Based on gluconate, the conversion is 65%. The mean experimental exchanged number of electrons ( $n_{exp}$ ) was evaluated by Equation (1).

$$n_{exp} = \frac{Q_{ox}}{FV\Delta c} \quad (1)$$

$$\tau_F = 100 \frac{n_{exp}(\text{experimental})}{n_{ex}(\text{theoretical})} \quad (2)$$

$$\tau = 100 \frac{n_{ex}FVc}{Q_{ox}} \quad (3)$$

in which  $Q_{ox}$  [C] is the involved quantity of electricity,  $\Delta c$  [mol L<sup>-1</sup>] =  $c_0 - c_f$ , which are the initial and final states for glucose,  $c$  [mol L<sup>-1</sup>] is the concentration of gluconate (peak A),  $V$  [L] is the volume of the electrolysis solution ( $V = 0.043$  L),  $F$  is the Faraday constant (96485 C mol<sup>-1</sup>),  $\tau_F$  is the Faradaic yield, and  $\tau$  is the catalyst efficiency.

If we assume that the theoretical exchanged number of electrons is  $n_{ex} = 2$  (gluconate, see above), the theoretical quantity of electricity is  $Q_{th} = 2 \times 0.02 \times 0.043 \times 96485 = 166$  C for full conversion (20 mM glucose). Consequently, the involved quantity of electricity after 7.5 h of electrolysis represents 74, 79, and 53% for glucose, galactose, and lactose, respectively. To obtain the time-dependent experimental number of electrons [Eq. (1)] and, subsequently, the experimental Faradaic yield [Eq. (2)], we performed the electrolysis of 50 mM glucose, and the results are reported in Figure 7b ( $\Delta c = c$ , from peak A) and Figure S9a–c. Only the intensity (Figure S9b) and the area (Figure S9c) of peak A increase significantly over time during electrolysis, and the contribution from this peak is very small (<10%; Figure S9c). At the end of the electrolysis,  $n_{exp} = 2.05$  for  $\tau_F = 102\%$ . Furthermore,  $n_{exp} = 2.2$  and  $\tau_F = 110\%$  were obtained for 20 mM glucose. A slight deviation of these values from theoretical ones ( $n_{exp} = 2$ ;  $\tau_F = 100\%$ ) was expected as the amount of peak B was considered [ $\Delta c = c$  was underestimated in Eq. (1)]. If we consider the electrolysis of 20 mM glucose

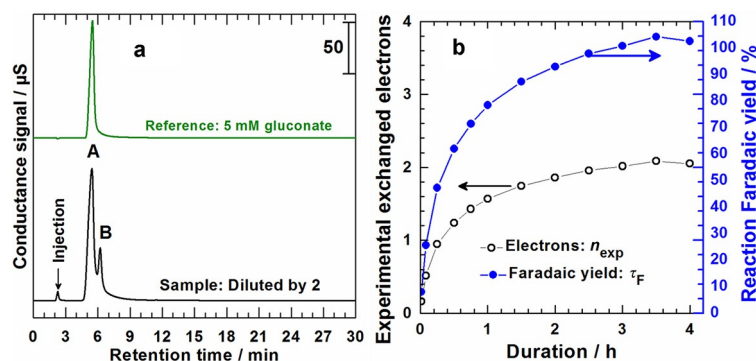


**Figure 7.** a) HPLIC chromatograms: reference (top) and analyte from the electrolysis of 20 mM glucose (bottom: diluted twice before injection). b) Experimental exchanged number of electrons (left y axis, black) and experimental Faradaic yield (right y axis, blue) based on the electrolysis of 50 mM glucose.

into 13 mM gluconate, the catalyst efficiency [Eq. (3)] is  $\tau = 88\%$ . This value is 89% towards galactonate (14 mM) if we consider galactose. The conversions obtained here (65–70%) are similar to those reported for heterogeneous catalysis.<sup>[3a,5d]</sup>

### Analytical investigation of the final reaction product

#### FTIRS and liquid chromatography coupled with mass spectrometry

To validate previous results, analytical analysis by FTIRS and liquid chromatography coupled with mass spectrometry (LC-MS) was performed. Experiments were performed after lyophilization in which a brown and sticky solid is obtained from glucose electrolysis, typical of gluconic acid.<sup>[5b,10a]</sup> This was firstly dissolved in 0.1 M NaOH to compare its FTIR spectrum with that of standards. Two FTIR spectra obtained under reproducible conditions are shown in Figure 8a. They confirm the IR

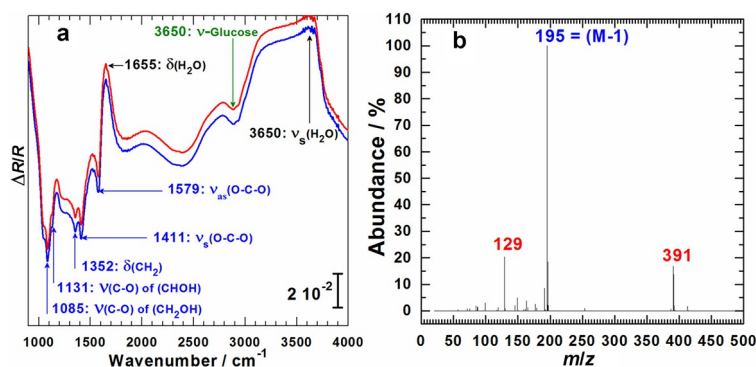


**Figure 8.** a) Two reproducible FTIR spectra of the product recorded in 0.1 M NaOH. b) LC-MS negative ionization mass spectrum (M-1) of the product.

bands of gluconate, which underpins the conclusion that gluconate is the main reaction product (based on the conclusions drawn from HPLIC). Furthermore, LC-MS enables us to distinguish different acids based on the mass of their pseudomolecular ions  $[M-H]^-$ :  $m/z = 209$  (glucaric), 195 (gluconic), and 193 (glucuronic) in negative-ionization mode (Figure S10). The spectrum from the LC-MS of the sample from glucose electrolysis is shown in Figure 8b. The peak at  $m/z = 195$  belongs to gluconic acid  $[M-H]^-$ , whereas those at  $m/z = 129$  and 391 are attributed to the fragmentation and simple dimerization processes. Spectra from galactose and lactose electrolyses are shown in Figure S10d and S10f, respectively. Consequently, the electro-oxidation of carbohydrates on Au/C concerns exclusively the C1-position and involves a two-electron process ( $n_{ex} = 2$ ). HPLIC and LC-MS are suitable methods for the accurate and effective determination of the final reaction products.

#### NMR spectroscopy

Qualitative NMR spectroscopy was performed to substantiate previous results. We especially focused on  $^{13}\text{C}$  NMR and  $^{13}\text{C}$  distortionless enhancement by polarization transfer (DEPT135)

NMR spectra, which offer a general fingerprint for carbon atoms at the C1-position. To obtain good NMR references, we first analyzed commercially available compounds: glucose (Figure S11 a–c), gluconate (from sodium gluconate, Sigma–Aldrich, Figure S12 a–d), and gluconolactone (Sigma–Aldrich, Figure S13 a–b). To mimic our experimental conditions in which gluconate is firstly obtained (electrolysis), then  $\text{H}^+$  exchanged (resin), and finally lyophilized, we used gluconate salt to generate gluconic acid (Figure S14 a–b). A comparison of NMR spectra ( $^1\text{H}$ ,  $^{13}\text{C}$ ,  $^{13}\text{C}$ -DEPT135,  $^1\text{H}$ - $^{13}\text{C}$ ) of gluconate before (Figure S12) and after lyophilization (Figure S14) indicates that the resin enables effective proton exchange.

As gluconic acid is available in solution (49–53 wt% in  $\text{H}_2\text{O}$ , Sigma–Aldrich), we lyophilized it firstly to remove water. Importantly, the  $^{13}\text{C}$  NMR spectrum of lyophilized gluconic acid solution (Figure 9a) and that of gluconate after  $\text{H}^+$  exchange and lyophilization (Figure S14a) are identical. The  $^{13}\text{C}$  NMR spectrum of the glucose electrolysis sample shown in Figure 9b (the obtained  $^{13}\text{C}$ -DEPT135 spectrum is reported in Figure S15) is the overlay of that from gluconate after  $\text{H}^+$  exchange and glucose (the conversion is not 100%). In particular, the  $^{13}\text{C}$  chemical shift of C1 is 95.9 and 92.1 ppm for  $\beta$ -glucose and  $\alpha$ -glucose, respectively. Quantification from Figure S11 a ( $^1\text{H}$  NMR) shows that  $\beta/\alpha = 75:25$  as expected.<sup>[18b]</sup> For gluconate, gluconic acid,  $\gamma$ -gluconolactone, and  $\delta$ -gluconolactone, the  $^{13}\text{C}$  chemical shift for C1 is 178.7, 176.9, 175.8, and 173.6 ppm in agreement previous reports.<sup>[20]</sup> ChemDraw simulations confirmed these shifts. As mentioned above, FTIRS analysis of the product (Figure 8a) did not disclose any gluconolactone specific band ( $\tilde{\nu} = 1742 \text{ cm}^{-1}$ ). Thus, we believe that the lyophilization induces partial gluconic acid cyclization into gluconolactone; a common phenomenon known as “lactonization”.<sup>[5b,20b,21]</sup> Then, gluconolactone is hydrolyzed swiftly into gluconate in  $\text{H}_2\text{O}/\text{NaOH}$  media (FTIRS conditions), which is contrary to that in  $\text{D}_2\text{O}$  media (NMR conditions) in which hydrolysis does not occur. For the first time, this rational and methodological study reveals that the GOR at the Au/C catalyst does not affect its carbon skeleton, and we assume that HPLIC peaks A and B belong both to gluconate.

#### Scheme of the electrocatalytic oxidation reaction

On the basis of all of our results, we can, therefore, resume glucose electro-oxidation in an alkaline medium on the Au nanocatalyst (Scheme 1). The reaction starts at an electrode potential  $E_1$  with glucose molecule adsorption through the  $\beta$ -hydrogen atom of C1 (good spatial arrangement,<sup>[18b]</sup>  $1^*$ ) and yields intermediate  $2^*$  (positive bands at  $\tilde{\nu} = 1030, 1050,$  and  $1080 \text{ cm}^{-1}$ ).<sup>[18b]</sup> The adsorption takes place at an active site denoted by “S”. S can be Au metal ( $E < 0.3 \text{ V vs. RHE}$ ),  $\text{Au}(\text{OH})_x$  ( $E > 0.3 \text{ V vs. RHE}$ ), or  $\text{AuO}_x$  ( $E > 1.2 \text{ V vs. RHE}$ ), which depends on the electrode potential.<sup>[16]</sup> For  $E > 0.3 \text{ V vs. RHE}$ , the participation of the catalyst in the GOR through  $\text{Au}(\text{OH})_x$  and/or  $\text{AuO}_x$  leads to the well-known bifunctional mechanism. At  $E_2 \geq E_1$ ,

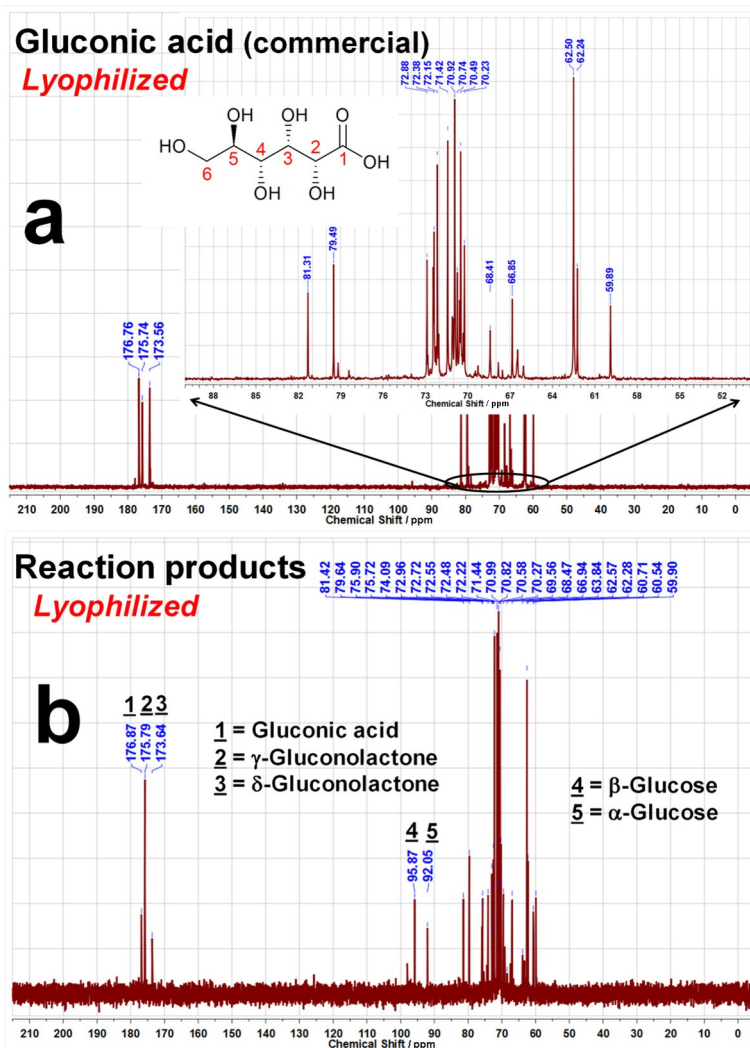


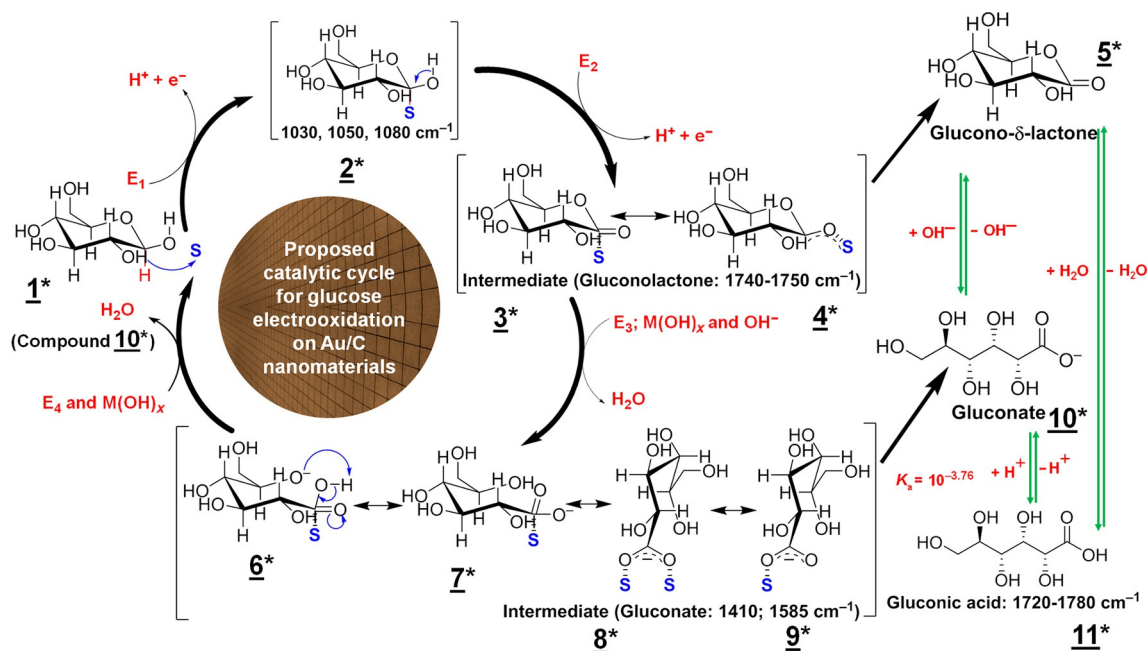
**Figure 9.**  $^{13}\text{C}$  NMR of a) lyophilized gluconic acid solution and b) the sample from glucose electrolysis after lyophilization.

the deprotonation of  $2^*$  leads to adsorbed gluconolactone ( $3^*/4^*$ ), which is quickly either desorbed ( $5^*$ ) or hydrolyzed into an alkoxide  $6^*$  at  $E_3$  ( $\geq E_2$ ) in the presence of hydroxides  $\text{M}(\text{OH})_x$  ( $\text{M}=\text{Au}$ ). This strong base undergoes self-rearrangement rapidly to yield adsorbed gluconate  $8^*/9^*$  ( $\tilde{\nu}=1412$  and  $1583\text{ cm}^{-1}$ ) via  $7^*$ . Desorption at  $E_4$  ( $\geq E_3$ ) in the presence of hydroxides  $\text{M}(\text{OH})_x$  gives gluconate in solution ( $10^*$ ) and, subsequently, releases fresh active sites  $5$  upon which a new glucose molecule can be adsorbed for further reaction. Depending on the pH value, gluconic acid ( $11^*$ ) can be observed ( $\tilde{\nu}=1720\text{--}1780\text{ cm}^{-1}$ ), and possible direct pathways can exist from  $5^*$  to  $10^*$  and/or  $11^*$ . The kinetics of each step depends undoubtedly on experimental conditions (temperature, concentration, etc.). Definitely, this reaction scheme could be more likely extended to other monosaccharides (e.g., galactose) than polysaccharides (e.g., lactose).

### Glucose alkaline fuel cell performances

For the DGFC, Au/C was used as the anode and Pt/C as the cathode catalyst. Pt/C exhibits impressive durability towards the ORR in an alkaline medium with only 12% loss in its electrochemical active surface after 1000 potential cycles from 0.05 to 1.1 V vs. RHE (Figure S16). In addition, it shows superior ORR performances than related carbon-supported electrocatalysts prepared by chemical methods.<sup>[11d]</sup> A photograph of the homemade DGFC is shown in Figure 10a, in which the AEM is fitted between the cathodic (+) and anodic (−) compartments (see the thin black layer).

We first examined whether our design enables ionic conductivity by recording CV in the three-electrode configuration (counter and working (together with reference) electrodes on either side of the membrane). The outcomes reported in Figure S17 show the efficiency of the constructed cell. The assembled fuel cell is shown in Figure 10b and c. The two black brushes on both ends (Figure 10b) show connections to the tiny reference electrodes (identical: SSCE). Meanwhile, blue (anode) and red (cathode) brushes show the electrode wiring, which enables us to display their OCP values on the corresponding multimeter screen (see video in SI). In 0.5 M KOH (pH 13.7), SSCE = +1005 mV vs. RHE. A bi-potentiostat (AUTO-LAB PGSTAT302N, Netherlands) was connected to the DGFC to monitor its OCV over time and then to record its polarization curves. The OCP (left y axis) and OCV (right y axis) measured over time (up to several hours) are shown in Figure 10d, and a steady-state was reached after a few minutes. Most studies of DGFCs used linear sweep voltammetry (LSV) to record polarization curves.<sup>[14,22]</sup> Basu and Basu reported that both LSV at a scan rate of  $1\text{ mVs}^{-1}$  and the common potentiostatic discharge method (PSD; steps of cell voltage ( $E_{\text{cell}}$ )) led to the same results.<sup>[22a]</sup> However, the scheduled program for our measurements was PSD with a step potential of 0.05 V between the OCV and 0.1 V after testing both methods (Figure S18). We also examined the effect of the supporting electrolyte with 0.1 M glucose (Figure S19). Despite the very high OCV of 1.1 V in 0.5 M NaOH compared to the OCV of 0.90 V in 0.5 M KOH, KOH allows us to deliver a higher current density supported by  $P_{\text{max}}=0.86\text{ mW cm}^{-2}$  compared to  $P_{\text{max}}=0.70\text{ mW cm}^{-2}$  for the NaOH electrolyte. We noted that this difference comes mostly from the cathode in which the potential decreases more quickly around the range of 0.9–0.7 V vs. RHE in 0.5 M NaOH. This has been ascribed to the contribution of  $\text{Na}^+$  and  $\text{K}^+$  ions on the ORR performances as KOH leads to better kinetics in the potential range of 0.9–0.8 V vs. RHE.<sup>[9a,23]</sup> During ORR studies, it is well known that the KOH electrolyte enables higher current densities to be obtained than NaOH. It should be indicated that an OCV of 1.1 V is the best value so far reported for such DGFCs.<sup>[6a,14,17a,22,24]</sup> We next assessed further features with the use of 0.5 M



**Scheme 1.** Proposed catalytic reaction cycle for glucose electro-oxidation in an aqueous medium on gold nanomaterials. S denotes the active site of gold that can be Au metal ( $E < 0.3$  V vs. RHE), Au(OH) $_x$  ( $E > 0.3$  V vs. RHE), or AuO $_x$  ( $E > 1.2$  V vs. RHE).  $E_i$  ( $i = 1-4$ ) is the electrode potential; M(OH) $_x$  is the hydroxyl species involved in the reaction (M = Au). Chemical equilibria indicated by green arrows between compounds 5\*, 10\*, and 11\* depend on the pH of the medium.

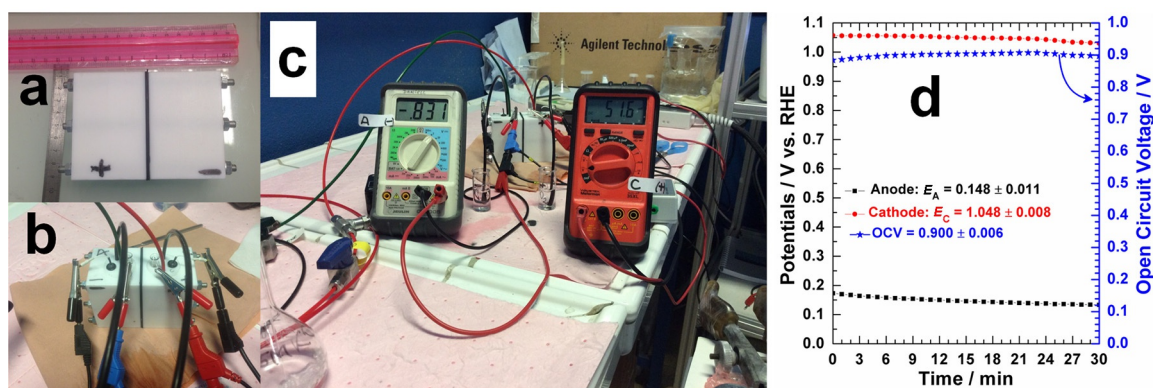


**Figure 10.** a) Photograph of the homemade fuel cell unit using an AEM fitted between the cathode (+) and anode (-) compartments (see the thin black layer). b) Photograph of the fuel cell that shows the different wiring (close view). c) Photograph taken during fuel-cell operation: multimeters show the potentials of the electrodes versus the reference electrode, SSCE (left for anode, white, and right for cathode, red). d) Left y axis: evolution over time of the anode and cathode potentials versus RHE; right y axis: measured OCV. Anode: 20 wt% Au/C (0.18 mg $_{Au}$  cm $^{-2}$ ); cathode 20 wt% Pt/C (0.17 mg $_{Pt}$  cm $^{-2}$ ); Fumatech AEM. Anode: 0.5 mol L $^{-1}$  KOH+0.3 mol L $^{-1}$  glucose (deoxygenated by N $_2$ ) and cathode: 0.5 mol L $^{-1}$  KOH+O $_2$  for measurements in c and d.

KOH. DGFC performances at different concentrations are presented in Figure 11 a and b (Figure S20). The OCV is quite similar, 0.90 V ( $\pm 20$  mV);  $P_{max} = 0.86$  (0.1 M), 1.43 (0.2 M), 2.02 (0.3 M), and 1.52 mW cm $^{-2}$  (0.4 M). The value of  $P_{max}$  of 2.02 mW cm $^{-2}$  for 0.3 M glucose obtained here for only 0.2 mg $_{Au}$  cm $^{-2}$  at 25 °C is highly improved (at least twofold) compared to 1.08 mW cm $^{-2}$  (1.2 mg $_{PtRu}$  cm $^{-2}$  at 30 °C),<sup>[25]</sup> 0.52 mW cm $^{-2}$  (0.45 mg $_{AuPtPd}$  cm $^{-2}$  at 30 °C),<sup>[22b]</sup> and 1.1 mW cm $^{-2}$  (0.6 mg $_{Au}$  cm $^{-2}$  at 30 °C),<sup>[22c]</sup> except the unpredictable value of 20 mW cm $^{-2}$  reached with an unrealistic metal loading of 3 mg $_{Pt}$  cm $^{-2}$  (0.5 M glucose, 30 °C).<sup>[14]</sup> Here the metal loading is

15-fold lower, and our Au/C catalyst is more stable than the Pt catalyst used there.

Furthermore, with the increase of the glucose concentration, higher current and power densities are expected because of the presence of a greater number of reacting molecules. This is the case for glucose concentrations up to 0.3 M. However, experimental results herein (Figure 11 a) and reported previously<sup>[8,22a,b,26]</sup> show that a too high glucose concentration is accompanied by a decrease in the cell performance. We believe that there are at least two rational reasons that explain the output power decrease for a certain limit of glucose concentra-

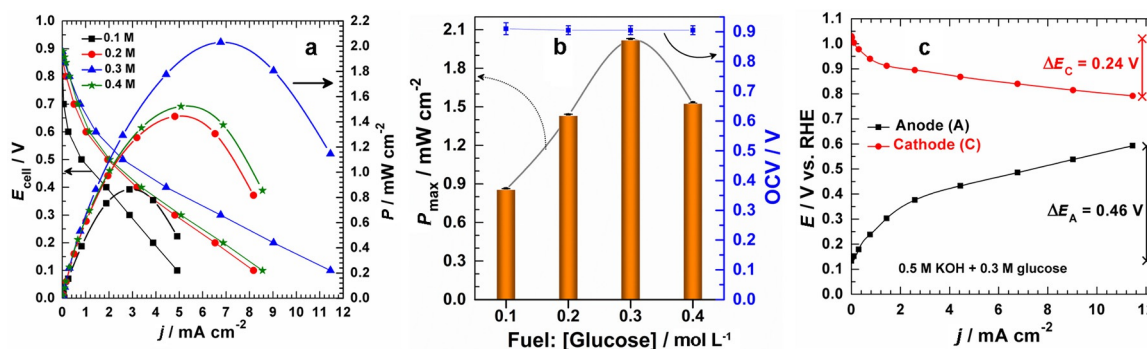


**Figure 11.** a) Fuel cell polarization curves for different concentrations of glucose in terms of cell voltage ( $E_{\text{cell}}$ ; left y axis) and power density ( $P$ ; right y axis). b) Effect of glucose concentration of the OCV (right y axis) and maximum power density ( $P_{\text{max}}$ ; left y axis). c) Typical behavior of the anode and cathode potentials recorded during the polarization curve measurements (0.3 M glucose). Anode: 20 wt% Au/C (0.18  $\text{mg}_{\text{Au}} \text{cm}^{-2}$ ); cathode 20 wt% Pt/C (0.17  $\text{mg}_{\text{Pt}} \text{cm}^{-2}$ ); Fueltech AEM. Anode: 0.5  $\text{mol L}^{-1}$  KOH+glucose (deoxygenated by  $\text{N}_2$ ); cathode: 0.5  $\text{mol L}^{-1}$  KOH+ $\text{O}_2$ .

tion. The first is the coverage rate of the electrode surface provided by adsorbed reactive molecules to lead to a competition between glucose molecules and hydroxyl ions. Indeed, the increase of the fuel concentration results in a saturation of the anode catalyst surface by excessively adsorbed glucose molecules. As the presence of adsorbed hydroxyl ( $\text{OH}_{\text{ads}}$ ) species is crucial for glucose oxidation,<sup>[16]</sup> the difficulty in their adsorption on the active sites may diminish the cell performance significantly. Similarly, an increase of the electrolytic solution (NaOH or KOH) concentration will provide more reacting  $\text{OH}^-$  species and enhance the kinetics of the glucose oxidation reaction (Figure S18d). However, a too high concentration of electrolyte ( $> 1 \text{ M}$ ) will lead to the degradation of the AEM and a decrease of the number of sites available for substrate (glucose molecules) adsorption at the anode.<sup>[22a, 26c]</sup> The second reason is related to the mass transport phenomenon: remove reaction products and route reactants to catalytic sites. It is known that the mass-transport phenomenon is one of the most limiting parameters for a fuel cell that uses an organic molecule as the fuel. The principle of mass transport, also referred to as a diffusion-limiting process, consists of bringing the reacting species close enough to the surface of the catalyst and removing the species formed at the surface into the bulk of the solution. Initially, an increase of the fuel concentration is accompanied by an increase in cell performances (Figure 11 a). However, a too high glucose concentration will lead to poor mass transport that may reduce the cell performances significantly. An increase of the fuel concentration increases the solution viscosity that can limit the transport of the fuel through the solution and catalytic layer toward the active sites at which the oxidation reaction occurs. With a molecule such as glucose, which has a low diffusivity ( $D=6.9 \times 10^{-10} \text{ m}^2 \text{ s}^{-1}$ ),<sup>[22a]</sup> especially in a batch cell in which no product outlet is provided, the decrease in cell performance with an increase in the glucose concentration after a certain limit is clear.<sup>[8, 22a, b, 26]</sup> Even if a flow cell is used, a decrease of the cell performances at high concentration is usually observed, and the validity of the two aforementioned hypotheses has been verified for a wide range of systems based on organic molecules (formic acid, methanol, ethanol, glycerol, etc.).<sup>[7e, 9b, 18c, 27]</sup>

Behavioral changes in the anode ( $E_{\text{A}}$ ) and cathode ( $E_{\text{C}}$ ) electrode potentials when the fuel cell delivers current were scrutinized thanks to our implanted SSCE reference electrodes. The recorded values for 0.3 M glucose are depicted in Figure 11 c. From  $E_{\text{cell}}=0.89$  (OCV) to 0.1 V,  $E_{\text{C}}$  goes from 1.03 to 0.79 V vs. RHE ( $\Delta E_{\text{C}}=0.24 \text{ V}$ ), and  $E_{\text{A}}$  undergoes a prominent increase from 0.13 to 0.59 V vs. RHE ( $\Delta E_{\text{A}}=0.46 \text{ V}$ ). Such results denote that performances are limited mostly by the anodic reaction as expected as the designed DGFC operates under batch conditions without fuel flow and the prompt removal of reaction products from electrodes. The future design of a flow-cell system might decrease the mass-transport limitation and lead to a better interaction between the reagents and the electrode surfaces.

## Conclusions

In this work, we aimed towards the electrochemical valorization of carbohydrates by using a direct alkaline fuel cell (DGFC). We scrutinized the fundamental aspects of the anode electrocatalytic reaction thoroughly by coupling electrochemical (cyclic voltammetry, chronoamperometry, electrolysis) to spectroscopic (cyclic voltammetry coupled with IR spectroscopy, NMR), spectrometric (LC-MS), and chromatographic (high-performance liquid ionic chromatography) methods. Au/C was the anode electrode material, and Pt/C was used on the cathodic side. Both were made by the “bromide anion exchange” approach with a good yield ( $> 90\%$ ). Characterization (TEM, X-ray photoelectron spectroscopy, XRD) reveals well-dispersed and unoxidized metal nanoparticles on the support. The judicious combination of (electro)analytical techniques allowed the unambiguous determination of the reaction product over the Au/C catalyst. Glucose was oxidized selectively without C–C bond cleavage to gluconate (which can be altered into gluconic acid on ion-exchange resin) contrary to previous reports. The Faradaic efficiency is nearly 100%. With the proposed reaction scheme, this work is a crucial step towards the electrosynthesis of organics without restrictive conditions as in organic chemistry synthesis.

In 0.5 M KOH and 0.3 M glucose, the DGFC has an open-circuit voltage of 0.9 V and delivers a maximum power of  $2.02 \text{ mW cm}^{-2}$ , which is at least twofold higher than the reported counterparts. Our findings underline that the fuel cell performances are limited by phenomena that occur at the anode, especially mass transport. Finally, the efficiency of the electrochemical production of energy and chemicals was demonstrated successfully by a high-output-power DGFC in which glucose is oxidized selectively at the anode. We are highly confident that upcoming improvements in cell design, namely, size, flow conditions, low surface resistance in a suitable membrane-electrode-assembly, and operating temperature, will lead to current and power increases for wide stationary applications. This work continues the research in which efforts are devoted to develop advanced, environmentally friendly energy converters and emphasizes that the cogeneration of clean energy and chemicals is utterly doable.

## Experimental Section

### Preparation of the nanocatalysts

The nanocatalysts used for the electrochemical conversion of glucose were prepared according to the BAE method<sup>[28]</sup> using carbon black (Vulcan XC 72R, Cabot, pretreated thermally to boost the electrocatalytic properties of the nanoparticles<sup>[29]</sup>) as the support (thereafter denoted as Au/C) for a targeted metal loading of 20 wt%. Basically, to prepare 100 mg of catalyst, tetrachloroauric(III) acid trihydrate ( $\text{HAuCl}_4 \cdot 3\text{H}_2\text{O}$ ; 40.0 mg; Sigma-Aldrich,  $\geq 99.9\%$ ) was dissolved in a reactor that contained ultrapure water (100 mL; MQ: Milli-Q Millipore,  $18.2 \text{ M}\Omega \text{ cm}$  at 293 K) at  $25^\circ\text{C}$  under stirring. This was followed by the addition of KBr (17.8 mg; Sigma-Aldrich,  $\geq 99\%$ ) under vigorous stirring. Then, carbon black (80 mg) was added under constant ultrasonic homogenization for 45 min. Afterwards, the metal salt was reduced by the addition of sodium borohydride (15 mL,  $0.1 \text{ mol L}^{-1} \text{ NaBH}_4$ ; Sigma-Aldrich, 99%) and the mixture was stirred vigorously at  $40^\circ\text{C}$  for 2 h. Finally, the carbon-supported gold nanoparticles were collected by filtration, washed several times with MQ water, and dried in an oven at  $40^\circ\text{C}$  for 12 h. The nanocatalyst was prepared with a synthesis yield of 94%. The Pt/C catalyst used as cathode electrode material was prepared in the same way using hexachloroplatinic(IV) acid hexahydrate ( $\text{H}_2\text{PtCl}_6 \cdot 6\text{H}_2\text{O}$ ; 53.1 mg; Sigma-Aldrich,  $\geq 37.50\%$  Pt basis) as metal precursor. The synthesis yield was 91% for the Pt/C catalyst.

### Nanomaterials characterization

The obtained nanomaterials were characterized physicochemically by TGA (real metal loading; by using a TA Instruments SDT Q-600 apparatus), XRD (crystallographic structure and crystallites size; by using an EMPYREAN (PANalytical) diffractometer in Bragg-Brentano  $\theta$ - $\theta$  configuration), TEM (morphology, particles size dispersion; by using a TEM/STEM JEOL 2100 UHR microscope at 200 kV), TEM coupled to EDX spectroscopy (elemental analysis; by using a JED Series AnalysisProgram, JEOL), and XPS (oxidation state of the surface; by using a Kratos Axis Ultra DLD spectrometer). Most of these techniques are described elsewhere.<sup>[29]</sup>

### (Spectro)electrochemical and analytical measurements

The catalyst ink was prepared by mixing MQ water (375  $\mu\text{L}$ ) and Nafion suspension (50  $\mu\text{L}$ ) in an ultrasonic bath (water). Then, catalyst powder (4 mg) was added to obtain a homogeneous ink (delay depends on the apparatus<sup>[30]</sup>).

**CV:** Electrochemical CV tests were conducted by using a conventional three-electrode cell using a potentiostat EG&G PARC Model 362 (Princeton Applied Research). The reference electrode was a RHE. The working electrode consisted of 3  $\mu\text{L}$  catalyst ink deposited onto a well-polished glassy carbon disk (GC:  $0.071 \text{ cm}^2$ ) through an abrasive disk with alumina powders of 1, 0.3, and  $0.05 \mu\text{m}$ . A slab of GC ( $6.48 \text{ cm}^2$ ) was used as the counter electrode. NaOH (97%) and glucose (D-(+)-glucose, 99.5%) from Sigma-Aldrich were used as the electrolyte solution and fuel, respectively.

**Spectroelectrochemical measurements:** Details of in situ FTIRS measurements by using a Bruker IFS 66v spectrometer are described elsewhere.<sup>[31]</sup> A slab of GC and RHE served as the counter and reference electrodes, respectively. The working electrode consisted of 3  $\mu\text{L}$  of catalyst ink deposited onto a GC disk (8 mm diameter). The amount of Nafion in the ink was halved to reduce its interference (total volume unchanged). A small amount of ink was thus deposited to avoid reducing the IR beam with carbon black absorption. Excellent reflectivity was obtained by pressing the working electrode against the  $\text{CaF}_2$  window to obtain a thin layer of electrolytic solution. Spectroelectrochemical analyses consist of coupling either CV to FTIRS (SPAIRS) or CA to FTIRS. CV-FTIRS consists of recording the electrode reflectivity  $R_e$  at different potentials  $E_i$  in steps of 0.05 V at  $1 \text{ mV s}^{-1}$ , whereas CA-FTIRS concerns spectrum acquisition every 3 min at a set electrode potential. A setup of the  $\mu$ -AUTOLAB Type III (Metrohm Autolab BV, Netherlands) potentiostat was used for electrochemistry and OPUS software (Bruker) was used for IR spectroscopy.

**Electrolysis and chromatographic analyses:** Electrolysis was performed by using a Pyrex two-compartment cell<sup>[19a]</sup> separated with a AEM (Fumasep FAA, Fumatech). The AEM preventing the contents from mixing from the two compartments and provides the current relay through ion exchange between the auxiliary electrode compartment (GC:  $1.5 \text{ cm} \times 7.2 \text{ cm}$ ) and that of the working electrode. The latter is a square plate (2 cm side) of Carbon Paper (Spectracarb 2050L-1050; Fuel Cell Store, TX), similar to Toray Carbon Paper 090. Ink (50  $\mu\text{L}$ ) was deposited onto each face of the electrode. A RHE was used as the reference electrode, which was in contact with the working electrode compartment by a Luggin bridge. This compartment was filled with 43 mL of solution, which was stirred slightly during electrolysis by a bar magnet located at the bottom of the solution. After preliminary tests, electrolyses were finally performed with a CA program by using a potentiostat EG&G PARC Model 362. This choice was motivated by the risk of having contaminants in the final products, some of which come from the catalytic surface regeneration at high potential. At the end of the electrolysis, the collected sample was divided into two parts. The first part was analyzed immediately by HPLIC (Dionex system ISC 5000) in gradient elution with a conductivity detector (CD-5000: allows the elution by conductivity strength) and an amperometric detector (ED-5000: allows in situ electrolysis for qualitative and quantitative analyses). The HPLIC included an autosampler (AS50 Automated Sample Injector), a sample loop (20  $\mu\text{L}$ ), and a column  $2 \times 250 \text{ mm}$  (IonPac AS15), which operated at  $30^\circ\text{C}$ . A constant flow of eluent ( $0.3 \text{ mL min}^{-1}$  at pressure of  $\approx 1500 \text{ psi}$ ) was provided by a pump (ICS-5000 P). The used eluent was

a 10 mmol L<sup>-1</sup> NaOH solution prepared from a concentrated stock solution (Acros Organics: 50 wt%, density = 1.5). The HPLIC was controlled by Chromeleon 6.80 software.

**Analytical analyses. Lyophilization, LC-MS, and NMR spectroscopy:** The second part of the electrolysis solution was passed through a cationic resin (DOWEX 50WX8-200 ion-exchange resin; Sigma-Aldrich) to remove salts and convert carboxylates to their protonated forms. The final filtrate was frozen and lyophilized (Freeze PowerDry LL 3000; Thermo Scientific) to remove water by sublimation. The LC-MS used an ion-exclusion column (HPX-87H, 30 cm, Aminex) in isocratic elution at 0.6 mL min<sup>-1</sup> (solvent: water with 0.2% formic acid) and a mass spectrometer Xevo Q-TOF from Waters (software: MassLinx, Waters) in negative-ionization mode (cone voltage: 20–40 V). NMR spectra were recorded at 297 K in D<sub>2</sub>O solvent by using a 400 MHz (<sup>1</sup>H) or 100 MHz (<sup>13</sup>C) instrument, employing standard software provided by the manufacturer (Bruker). Various techniques were used to improve assignments: <sup>1</sup>H, <sup>13</sup>C, <sup>1</sup>H-<sup>1</sup>H (COSY), <sup>1</sup>H-<sup>13</sup>C (HSQC), and DETP 135 NMR.

### Direct glucose alkaline fuel cell design

A homemade two-compartment Teflon cell (with the same AEM as for electrolysis) operated under batch conditions was designed for DGFC tests (Figure 10). The electrode was a 1 cm<sup>2</sup> square plate (using both sides: 2 cm<sup>2</sup>) of Carbon Paper. Catalyst ink was prepared similarly to that used for CV. The anode catalyst was 20 wt% Au/C (0.18 mg<sub>Au</sub> cm<sup>-2</sup>), and the cathode catalyst was 20 wt% Pt/C (0.17 mg<sub>Pt</sub> cm<sup>-2</sup>). "BASi Reference Electrodes, 3 cm" (RE-6 Ag/AgCl, MF-2078) purchased from Alvatek Ltd (UK) with a flexible wire connector were used to follow each electrode potential.

### Acknowledgements

This research was supported by the French National Research Agency (ANR) in the framework of the "ChemBio-Energy program 2012–2015" including IC2MP and EBI. The authors are grateful to Dr. Jérôme Désiré (University of Poitiers) for useful discussions during NMR analyses.

**Keywords:** carbohydrates · electrochemistry · energy conversion · fuel cells · heterogeneous catalysis

[1] a) B. C. H. Steele, A. Heinzel, *Nature* **2001**, *414*, 345–352; b) J. Greeley, N. M. Markovic, *Energy Environ. Sci.* **2012**, *5*, 9246–9256.  
 [2] a) S. Chu, A. Majumdar, *Nature* **2012**, *488*, 294–303; b) M. Bellini, M. Bevilacqua, J. Filippi, A. Lavacchi, A. Marchionni, H. A. Miller, W. Oberhauser, F. Vizza, S. P. Annen, H. Grützmacher, *ChemSusChem* **2014**, *7*, 2432–2435.  
 [3] a) G. D. Watt, *Renewable Energy* **2014**, *72*, 99–104; b) J. McGinley, F. N. McHale, P. Hughes, C. N. Reid, A. P. McHale, *Biotechnol. Lett.* **2004**, *26*, 1771–1776.  
 [4] A. M. Ruppert, K. Weinberg, R. Palkovits, *Angew. Chem. Int. Ed.* **2012**, *51*, 2564–2601; *Angew. Chem.* **2012**, *124*, 2614–2654.  
 [5] a) I. Dencic, J. Meuldijk, M. Croon, V. Hessel, *J. Flow Chem.* **2011**, *1*, 13–23; b) S. Ramachandran, P. Fontanille, A. Pandey, C. Larroche, *Food Technol. Biotechnol.* **2006**, *44*, 185–195; c) M. Varničić, T. Vidaković-Koch, K. Sundmacher, *Electrochim. Acta* **2015**, *174*, 480–487; d) P. Qi, S. Chen, J. Chen, J. Zheng, X. Zheng, Y. Yuan, *ACS Catal.* **2015**, *5*, 2659–2670.  
 [6] a) E. H. Yu, X. Wang, U. Krewer, L. Li, K. Scott, *Energy Environ. Sci.* **2012**, *5*, 5668–5680; b) N. Fujiwara, Z. Siroma, S.-i. Yamazaki, T. Ioroi, H. Senoh, K. Yasuda, *J. Power Sources* **2008**, *185*, 621–626.

[7] a) Y.-J. Wang, J. Qiao, R. Baker, J. Zhang, *Chem. Soc. Rev.* **2013**, *42*, 5768–5787; b) H. Zhang, P. K. Shen, *Chem. Rev.* **2012**, *112*, 2780–2832; c) J. R. Varcoe, P. Atanassov, D. R. Dekel, A. M. Herring, M. A. Hickner, P. A. Kohl, A. R. Kucernak, W. E. Mustain, K. Nijmeijer, K. Scott, T. Xu, L. Zhuang, *Energy Environ. Sci.* **2014**, *7*, 3135–3191; d) E. H. Yu, U. Krewer, K. Scott, *Energies* **2010**, *3*, 1499; e) R. Pathak, S. Basu, *Electrochim. Acta* **2013**, *113*, 42–53.  
 [8] A. Ilie, M. Simoes, S. Baranton, C. Coutanceau, S. Martemianov, *J. Power Sources* **2011**, *196*, 4965–4971.  
 [9] a) A. Wieckowski, E. R. Savinova, C. G. Vayenas, *Catalysis and Electrocatalysis at Nanoparticle Surfaces*, Marcel Dekker, Inc., New York, **2003**; b) H. Corti, E. R. Gonzalez, *Direct Alcohol Fuel Cells*, Springer Netherlands, Dordrecht, **2014**.  
 [10] a) P. M. Collins, *Dictionary of Carbohydrates, 2nd ed.*, Chapman & Hall/CRC, London, **2006**; b) R. K. Thauer, K. Jungermann, K. Decker, *Bacteriol. Rev.* **1977**, *41*, 100–180.  
 [11] a) M. K. Debe, *Nature* **2012**, *486*, 43–51; b) L. Su, W. Jia, C.-M. Li, Y. Lei, *ChemSusChem* **2014**, *7*, 361–378; c) A. Anastasopoulos, J. C. Davies, L. Hannah, B. E. Hayden, C. E. Lee, C. Milhano, C. Mormiche, L. Offin, *ChemSusChem* **2013**, *6*, 1973–1982; d) Y. Holade, N. Sahin, K. Servat, T. Napporn, K. Kokoh, *Catalysts* **2015**, *5*, 310–348; e) J. Greeley, I. E. L. Stephens, A. S. Bondarenko, T. P. Johansson, H. A. Hansen, T. F. Jaramillo, J. Rossmeisl, I. Chorkendorff, J. K. Nørskov, *Nat. Chem.* **2009**, *1*, 552–556; f) J. Kibsgaard, Y. Gorlin, Z. Chen, T. F. Jaramillo, *J. Am. Chem. Soc.* **2012**, *134*, 7758–7765; g) Y. Zhang, Y.-C. Hsieh, V. Volkov, D. Su, W. An, R. Si, Y. Zhu, P. Liu, J. X. Wang, R. R. Adzic, *ACS Catal.* **2014**, *4*, 738–742.  
 [12] L. Mor, Z. Rubin, P. Schechner, *J. Fuel Cell Sci. Technol.* **2008**, *5*, 014503–014503.  
 [13] a) E. Katz, K. MacVittie, *Energy Environ. Sci.* **2013**, *6*, 2791–2803; b) W. Gellert, M. Kesmez, J. Schumacher, N. Akers, S. D. Minteer, *Electroanalysis* **2010**, *22*, 727–731; c) D. P. Hickey, F. Giroud, D. W. Schmidtke, D. T. Glatzhofer, S. D. Minteer, *ACS Catal.* **2013**, *3*, 2729–2737.  
 [14] N. Fujiwara, S.-i. Yamazaki, Z. Siroma, T. Ioroi, H. Senoh, K. Yasuda, *Electrochem. Commun.* **2009**, *11*, 390–392.  
 [15] K. Juodkazis, J. Juodkazyt, V. Jusulaitien, A. Lukinskas, B. Šebeka, *Electrochem. Commun.* **2000**, *2*, 503–507.  
 [16] a) M. W. Hsiao, R. R. Adžić, E. B. Yeager, *J. Electrochem. Soc.* **1996**, *143*, 759–767; b) M. Pasta, R. Ruffo, E. Falletta, C. M. Mari, C. Della Pina, *Gold Bull.* **2010**, *43*, 57–64; c) S. Hebié, L. Cornu, T. W. Napporn, J. Rousseau, B. K. Kokoh, *J. Phys. Chem. C* **2013**, *117*, 9872–9880; d) S. Hebié, Y. Holade, K. Maximova, M. Sents, P. Delaporte, K. B. Kokoh, T. W. Napporn, A. V. Kabashin, *ACS Catal.* **2015**, *5*, 6489–6496.  
 [17] a) D. Basu, S. Basu, *Int. J. Hydrogen Energy* **2011**, *36*, 14923–14929; b) C. Zhu, S. Guo, S. Dong, *Adv. Mater.* **2012**, *24*, 2326–2331; c) L. Yan, A. Brouzgou, Y. Meng, M. Xiao, P. Tsiakaras, S. Song, *Appl. Catal. B* **2014**, *150–151*, 268–274.  
 [18] a) P. Tonda-Mikiela, T. W. Napporn, C. Morais, K. Servat, A. Chen, K. B. Kokoh, *J. Electrochem. Soc.* **2012**, *159*, H828–H833; b) F. Largeaud, K. B. Kokoh, B. Beden, C. Lamy, *J. Electroanal. Chem.* **1995**, *397*, 261–269; c) Y.-L. Yang, X.-H. Liu, M.-Q. Hao, P.-P. Zhang, *Int. J. Hydrogen Energy* **2015**, *40*, 10979–10984; d) K. B. Kokoh, J. M. Léger, B. Beden, H. Huser, C. Lamy, *Electrochim. Acta* **1992**, *37*, 1909–1918.  
 [19] L. H. E. Yei, B. Beden, C. Lamy, *J. Electroanal. Chem. Interfacial Electrochem.* **1988**, *246*, 349–362.  
 [20] a) V. H. Pomin in *Glycosylation* (Ed.: S. Petrescu), INTECH, Rijeka, **2012**, pp. 63–98; b) J.-C. Portais, P. Tavernier, I. Besson, J. Courtois, B. Courtois, J.-N. Barbotin, *FEBS Lett.* **1997**, *412*, 485–489; c) C. S. Tsai, H. G. Ye, J. L. Shi, *Arch. Biochem. Biophys.* **1995**, *316*, 155–162.  
 [21] a) Z. Zhang, P. Gibson, S. Clark, G. Tian, P. Zanonato, L. Rao, *J. Solution Chem.* **2007**, *36*, 1187–1200; b) Y. Pocker, E. Green, *J. Am. Chem. Soc.* **1973**, *95*, 113–119.  
 [22] a) D. Basu, S. Basu, *Electrochim. Acta* **2011**, *56*, 6106–6113; b) D. Basu, S. Basu, *Int. J. Hydrogen Energy* **2012**, *37*, 4678–4684; c) L. Li, K. Scott, E. H. Yu, *J. Power Sources* **2013**, *221*, 1–5.  
 [23] a) N. M. Marković, P. N. Ross, *Surf. Sci. Rep.* **2002**, *45*, 117–229; b) N. M. Marković, H. A. Gasteiger, P. N. Ross, *J. Phys. Chem.* **1996**, *100*, 6715–6721; c) M. Nesselberger, S. Ashton, J. C. Meier, I. Katsounaros, K. J. J. Mayrhofer, M. Arenz, *J. Am. Chem. Soc.* **2011**, *133*, 17428–17433.  
 [24] C.-C. Chen, C.-L. Lin, L.-C. Chen, *J. Power Sources* **2015**, *287*, 323–333.  
 [25] D. Basu, S. Basu, *Electrochim. Acta* **2010**, *55*, 5775–5779.

- [26] a) R. L. Arechederra, B. L. Treu, S. D. Minter, *J. Power Sources* **2007**, *173*, 156–161; b) Y. S. Li, T. S. Zhao, Z. X. Liang, *J. Power Sources* **2009**, *187*, 387–392; c) C. Rice, S. Ha, R. I. Masel, P. Waszczuk, A. Wieckowski, T. Barnard, *J. Power Sources* **2002**, *111*, 83–89.
- [27] a) C. A. Apblett, D. Ingersoll, S. Sarangapani, M. Kelly, P. Atanassov, *J. Electrochem. Soc.* **2010**, *157*, B86–B89; b) F. M. Cuevas-Muñiz, M. Guerra-Balcázar, J. P. Esquivel, N. Sabaté, L. G. Arriaga, J. Ledesma-García, *J. Power Sources* **2012**, *216*, 297–303.
- [28] Y. Holade, C. Morais, S. Arrii-Clacens, K. Servat, T. W. Napporn, K. B. Kokoh, *Electrocatalysis* **2013**, *4*, 167–178.
- [29] Y. Holade, C. Morais, K. Servat, T. W. Napporn, K. B. Kokoh, *Phys. Chem. Chem. Phys.* **2014**, *16*, 25609–25620.
- [30] B. G. Pollet, *Electrocatalysis* **2014**, *5*, 330–343.
- [31] Y. Holade, C. Morais, K. Servat, T. W. Napporn, K. B. Kokoh, *ACS Catal.* **2013**, *3*, 2403–2411.

---

Received: December 1, 2015

Published online on January 18, 2016